Article

Miniaturized and Circularly Polarized Dual-Port Metasurface-Based Leaky-Wave MIMO Antenna for CubeSat Communications

Tale Saeidi [1,2,*], Sahar Saleh [1,3,*] and Saeid Karamzadeh [4,5]

1 WiSAR Lab, Atlantic Technological University (ATU), F92 FC93 Letterkenny, Ireland
2 Electrical and Electronics Engineering Department, Faculty of Engineering and Natural Sciences, İstinye University, 34396 Istanbul, Turkey
3 Department of Electronics and Communications Engineering, Faculty of Engineering, Aden University, Aden 5243, Yemen
4 Millimeter Wave Technologies, Intelligent Wireless System, Silicon Austria Labs (SAL), 4040 Linz, Austria; saeid.karamzadeh@silicon-austria.com
5 Electrical and Electronics Engineering Department, Faculty of Engineering and Natural Sciences, Bahçeşehir University, 34349 Istanbul, Turkey
* Correspondence: tale.saeidi@atu.ie (T.S.); sahar.saleh@atu.ie (S.S.)

Abstract

This paper presents a compact, high-performance metasurface-based leaky-wave MIMO antenna with dimensions of 40×30 mm^2, achieving a gain of 12.5 dBi and a radiation efficiency of 85%. The antenna enables precise control of electromagnetic waves, featuring a flower-like metasurface (MTS) with coffee bean-shaped arrays on substrates of varying permittivity, separated by a cavity layer to enhance coupling. Its dual-port MIMO design boosts data throughput operating in three bands (3.75–5.25 GHz, 6.4–15.4 GHz, and 22.5–30 GHz), while the leaky-wave mechanism supports frequency- or phase-dependent beamsteering without mechanical parts. Ideal for CubeSat communications, its compact size meets CubeSat constraints, and its high gain and efficiency ensure reliable long-distance communication with low power consumption, which is crucial for low Earth orbit operations. Circular polarization (CP) maintains signal integrity despite orientation changes, and MIMO capability supports high data rates for applications such as Earth observations or inter-satellite links. The beamsteering feature allows for dynamic tracking of ground stations or satellites, enhancing mission flexibility and reducing interference. This lightweight, efficient antenna addresses modern CubeSat challenges, providing a robust solution for advanced space communication systems with significant potential to enhance satellite connectivity and data transmission in complex space environments.

Keywords: CubeSat; LWA; metasurface; multi-band MIMO antenna; beamsteering; LEO

1. Introduction

Satellite technologies, particularly CubeSats, have advanced space exploration, enabling economical missions for communication, Earth observation, and scientific research. The satellites, with dimensions likely to be $10 \times 10 \times 10$ cm^3 per unit, require lightweight, compact components with low power consumption to meet requirements such as strict size, weight, and power (SWaP) constraints while sustaining solid performance in severe space conditions. Antennas, as vital components of any CubeSat communication system, serve as a key connection for transmitting data between the satellite and ground stations

or other satellites [1]. Nevertheless, ordinary antenna designs, such as reflectors with parabolic shapes and those that can be mechanically steered, may be frequently impractical for CubeSat systems because of their sophisticated, bulky constructions, and MTS-based antennas might be solutions [2,3]. To have applicable space communication, antennas designed for CubeSat communications must fulfill the size and weight requirements for units up to $10 \times 10 \times 10$ cm^3 (1U) [4].

Apart from being lightweight and miniaturized, antennas designed for CubeSats should also be deployable and offer a higher gain while being packed sufficiently during both launch and in orbit. Various frequency bands were utilized for satellite communications based on the International Telecommunication Union (ITU) and global satellite communication regulations, including Very High Frequency (VHF), Ultra High Frequency (UHF), the S band, and the X band [5]. The antenna used for space missions should either emit in all directions, which is crucial for low Earth orbit (LEO) missions, ensuring a stable connection regardless of alignment, or be directional, having a high gain to concentrate energy and boost communication reliability [6]. The antenna designed for CubeSat should have key factors, including polarization (circular polarization is preferred due to its robustness towards misalignment, unlike linear polarization, which works for exact positioning), high efficiency (to have an efficient onboard power), and acceptable bandwidth (BW) (to function efficiently and adequately for telemetry, commands, and data downlinks). In addition to these factors, they should also have low-power functionality (which is vital given CubeSats' limited energy reserves); they should exhibit environmental durability so they can endure space's extreme temperatures and radiation for sustained performance; their structure should be strong enough so they can resist launch-related vibrations and shocks; they should have multi-role capabilities, like multi-band systems, having the least interference so as not to have conflicts with other systems; and they should be cost-effective. Considering these requirements and factors, the following research and designed antennas were conducted and proposed for CubeSat and broader satellite communication applications. In addition to the aforementioned factors, CubeSat communication antennas should also possess beamsteering capabilities. Various antennas have been designed and employed for CubeSat communications, considering beamsteering, including planar-phased patch antennas [7], dielectric lenses and reflectors [8], leaky-wave antennas, reconfigurable antennas, and MTS antennas [9].

The following subsections provide a comprehensive review of the current state of the art in CubeSat antenna design, highlighting various types and configurations, along with their respective advantages and limitations. By investigating these designs and their gaps, the contributions of our study are explained.

1.1. The State of the Art and Analyses

This subsection presents the current state of the art in antenna design and analyses of their performance in CubeSat communications. According to the research in [10], a compact stacked-patch antenna with a wide frequency range was developed for a 3U CubeSat communication system, operating in the S band. The authors improved efficiency by using a special slot couple feed method with a cavity for E-field optimization, which improves the link between the feeding and radiating parts. The antenna achieved a gain increase of 9 dBi, redirecting backward radiation, and demonstrated a broad bandwidth of 32.6%, spanning 0.8 GHz. CubeSat systems operating at S-band frequencies are usually bulky, especially when configured as arrays. To address this issue, the authors in Ref. [11] designed a foldable microstrip patch antenna (MPA) with fractal shapes for 1U CubeSats. They constructed a miniaturized antenna without sacrificing high gains and achieved a smaller S$_{11}$ and a broad bandwidth by incorporating a Koch snowflake fractal pattern. Their

design also incorporates an uncomplicated deployment technique, operating at 2.3 GHz. The antenna exhibited an impressive reflection coefficient of -28 dB and a substantial bandwidth of 28.7% while delivering a decent gain of 4.39 dBi. The antenna's compactness ($60 \times 26.3 \times 0.02$ mm^3) is its primary advantage; however, its omnidirectional radiation pattern resulted in a lower gain, a notable downside.

Ref. [12] presented a square-shaped, compact, planar dipole antenna designed for 1U CubeSats, introducing four-element arrays interconnected via a phase-shifting network, and a balun was strategically placed to ensure even power distribution. It offered CP, preserving steady communication despite the CubeSat's orientation shifting with the dimensions of 55×55 mm^2. It provided bidirectional radiation, a significant 33.46% bandwidth, and a gain of 3.49 dBi, which surpassed the dipole antenna's performance in Ref. [13]. A small-scale X-band antenna, functioning in the 7.89–10.49 GHz band, achieved a remarkable gain of up to 35 dB. Another antenna utilized a split ring resonator (SSR) structure to operate at the X band. It was fabricated using chemical etching, and its performance was evaluated. The possibility of using this antenna as part of an array was investigated to enhance signal transmissions and reception gains [14]. Moreover, a compact, inverted S-shaped patch antenna was designed to operate at three X-band frequencies. It delivered bandwidths of 5.02%, 9.13%, and 3.79% across these respective bands. Its gain was enhanced by incorporating elliptical slots into the ground plane, and strong agreement was shown between the simulated and measured results. It also demonstrated stable gains and omnidirectional radiation, making it highly suitable for X-band applications [15].

An MPA with a rectangular slot and a defected ground structure (DGS) was designed for multi-band functionality, achieving notable gains across the C-, X-, and Ku-bands. It performed reliably at frequencies such as 6.035 GHz (GNSS), 6.795 GHz (satellite TV), 7.46 GHz (long-distance communication), 8.505 GHz (radar), 11.45 GHz (space communication), 13.35 GHz (detector), 15.06 GHz (military), 17.24 GHz (aerospace), and 19.05 GHz (astronomical observation). Cutting slots offered a quad-band resonance without altering the ground or patch. By cutting further and optimizing the slot size, a peak gain of 14.679 dBi was achieved in the upper-frequency band at 16 GHz [16]. A small-scale microstrip antenna was designed for dual-band operation in the S- and X-bands. It delivered bandwidths of 13% in the S band and 6.2% in the X band (reflection coefficient <-10 dB), with isolation exceeding 38 dB by employing electromagnetic coupling. It also offered gains of 7.5 dBi for the S band and 10.5 dBi for the X band [17]. A method to eliminate higher-order modes in microstrip antennas operating at single or dual frequencies was developed by integrating a microstrip filter directly into the antenna design, simplifying the transmitter and receiver systems. By offering a dual-frequency antenna for S and X bands, providing a 7% bandwidth and an 8 dBi gain in the S band and a 10.5% bandwidth with an 11.5 dBi gain in the X band, it may be well-suited for satellite communication systems [18].

In Ref. [19], a compact planar Yagi–Uda antenna was developed for PicoSats and small satellite missions, addressing size constraints through meandering and one-dimensional artificial dielectric techniques to fit within the small dimensions of these satellites. It operates at 3.46–3.54 GHz, and good agreement exists between the simulation and measurement results. The study demonstrated the compactness of the antenna and also how antenna systems support rapid communication in small satellite platforms. Ref. [20] introduced a substrate-integrated waveguide (SIW) antenna for CubeSats, utilizing middle-point feeding and shorting walls to achieve broadside radiation at dual frequencies. Communication flexibility was improved by offering a stable radiation pattern and also achieved a low profile, keeping it within CubeSat's size constraints. Its broadside radiation pattern assured a reliable signal transmission, offering a viable solution for enhanced small satellite communication. In Ref. [21], an innovative planar leaky-wave antenna (LWA) was introduced

to improve CubeSat communication, utilizing SIW technology with periodic fan-shaped slots etched on the SIW surface to achieve effective CP radiation. This design is highly advantageous for CubeSats, offering a compact and lightweight solution that meets the size, weight, power, and thermal (SWaP) constraints of small satellites with its high gain and broadside radiation pattern. A Fabry–Perot cavity (FPC) antenna was presented, featuring increased gains, a wide bandwidth, and CP to enhance data transfer for CubeSat and small satellite applications. Its high performance was achieved by employing a spatially distinct superstrate excitation method, and it meets SWaP limits. All results were evaluated through practical investigations and presented as significant for a small satellite field [22].

Slot antennas typically consist of flat metallic plates with strategically placed cuts within the frequency range of 0.3–25 GHz. Nonetheless, their power and directivity do not meet the CubeSat communication requirements. After exploring various possible methods, they can achieve a gain of 9.71 dBi and 30.2% of BW [23]. However, their primary drawback is their relatively large size. Ref. [24] presented a MTS antenna designed for RF energy harvesting with static beamsteering achieved through fixed metal slots and a secondary MTS layer. It functions at 2.4 GHz and offers an 8.1 dBi gain, but it is yet to have beamsteering abilities, despite its sophisticated structure.

An electronically steered MTS antenna developed by [25] operated at 10 GHz with a 9.6–10 GHz bandwidth, utilizing a 12×12 cm^2 aperture comprising 96 varactor-tuned elements spaced at half-wavelength intervals. This design achieved 2D beamsteering without traditional phase shifters, employing feed phase diversity and varactor diodes for continuous phase tuning. However, this antenna's reliance on varactors introduced nonlinearities and potential thermal instability, and its 12×12 cm^2 size was relatively large. Biasing the varactors required too much power, and the feeding network further enhanced complexity, which is contrary to the simplicity and power constraints of CubeSats. An antenna with two vertically faced MTSs resonating at 26.8 GHz, offering polarization-independent unit cells capable of absorption, reflection, and a 180° phase shift within the 26.5–27 GHz band, was introduced in [26]. This antenna utilized a $2 \times 14 \times 14$ array with PIN diodes for mode switching and employed genetic algorithms for phase optimization. It offered 1-bit phase quantization and a limited beam resolution and had a complex multilayer structure with numerous active components, which increased its size, power consumption, and thermal management challenges.

A dual-port, dual-beam, pattern-reconfigurable antenna operating at 3.6 GHz with a bandwidth over 400 MHz, achieving 360° azimuth and 60° elevation scanning, was developed by Ref. [27]. This design employed reconfigurable metal lines (RMLs) with PIN diodes, offering independent 2D beam control per port, and delivered an average gain of 8 dBi, up to 80% efficiency, and port isolation of more than 20 dB. However, the complexity of the systems increased, as well as their weight, power consumption, and costs. Thus, while effective for terrestrial applications, this design is not optimal for CubeSat communications. Ref. [28] introduced another reconfigurable electromechanical reflectarray (REMR) antenna operating at 5.5 GHz, which employed cam-actuated ground plane displacements to achieve continuous phase shifts of up to 200°, enabling beamsteering across incidence angles ranging from 0° to 70°. The design eliminated the need for active electronics, offering low-loss performance and mechanical stability, even when powered off. However, the mechanical actuators introduced some problems in the harsh space environment due to latency, and the potential reliability may not be ideal for CubeSat platforms. Lastly, Ref. [29] developed a passive multibeam antenna for CubeSat applications, operating at 39 GHz within the Ka-band. This design integrated a 2D microstrip antenna array with a 3D-printed half-ellipsoid lens, enabling beam selection across 16 discrete directions. The antenna achieved gains between 14 and 16 dBi with half-power beam widths ranging from

14° to 18°, and the lens weighs approximately 15.2 g. While 3D printing offers a cost-effective and lightweight solution, the reliance on discrete beam switching limits real-time adaptability, and the physical size of the lens poses integration challenges that may not be optimal for CubeSat communications, despite this innovative approach. A detailed comparison of research presented in this state-of-the-art section is presented in Table 1.

Table 1. The state of the art of recent antennas designed for CubeSat communications.

References	f_r (GHz)	Size (mm × mm)	Gain (dBi)	Polarization	Efficiency (%)	Antenna Type	Application
[10]	2	12 × 12	3	N/A	N/A	Patch antenna	CubeSat
[11]	2.3, 2.4, and 2.45	6 × 26.30	4.39	N/A	N/A	Fractal antenna	CubeSat
[12]	2.4	55 × 55	3.49	CP	N/A	Planar	Pico satellite
[13]	2.5	N/A	5.03	N/A	N/A	Dipole	CubeSats
[14]	7.89–10.49	N/A	35	N/A	N/A	Microstrip patch	Space communication
[15]	10.47–11.4	20 × 17.2	<5	N/A	<97	Microstrip patch	X-band applications
[16]	6.0350, 6.7950, 7.46, 8.5050, 11.45, 13.35, 15.06, 17.24, and 19.05	22 × 27	14.4	Linear	N/A	Microstrip patch	C- and X-band applications
[17]	2.4–2.63 7.7–8.5	95 × 95	10.5	N/A	N/A	Microstrip patch	S/X-bands
[18]	2.5 and 8	140 × 140	11.5	N/A	N/A	Microstrip patch	S/X-communications
[19]	2.4	90 × 51.5	5	N/A	N/A	Planar Yagi–Uda	PicoSat and CubeSat
[20]	23.2–23.5 and 24.8–25.2	20 × 12	8	LP	87	LWA	CubeSat
[21]	27.4–37.3	107 × 17	17.9	CP	89	LWA	CubeSat
[22]	7.99–9.02	80 × 80	15.73	CP	N/A	Fabry–Perot cavity	CubeSat
[23]	2.45	90 × 90	9.71	CP	N/A	CPW–fed slot antenna	CubeSat
[24]	12.5	N/A	N/A	N/A	N/A	Metasurface antenna	Frequency energy harvesting
[25]	10	229 × 229	<10	N/A	11	Metasurface antenna	N/A
[26]	26.5–27	26 × 26	N/A	N/A	N/A	Metasurface	N/A
[27]	3.6	80 × 80	8	Orthogonal	>80	Reconfigurable antenna	Beam-scanning
[28]	sub-6 GHz	400 × 441	N/A	N/A	N/A	Reflectarray antenna	Beamsteering
[29]	39	37 × 30.96	16	N/A	53	3D-printed lens	Ka-band CubeSat

1.2. Contributions of This Study

This study proposes a miniaturized MTS-based leaky-wave MIMO antenna optimized for CubeSat communication systems across microwave and millimeter-wave bands. The antenna features a compact, dual-port MIMO design using a modified phased MTS with coffee bean-shaped arrays. The MTS arrays were embedded on a substrate with a different permittivity, which was separated by a cavity layer to have improved propagation. This specific construction can offer beamsteering abilities with frequency and phase dependency, which is vital for CubeSat communications. The antenna operates over three bands, 3.75–5.25 GHz, 6.4–15.4 GHz, and 22.5–30 GHz, and is designed to fit within the standard $10 \times 10 \times 10$ cm^3 CubeSat unit, preserving space for other critical systems, like solar panels. In addition, its high gain and radiation efficiency of 12.5 dBi and 85%, respectively, and also its circular polarization can assure low power consumption and a robust signal reception, which are essential for low Earth orbit (LEO). Overall, the antenna meets the stringent size, weight, and power (SWaP) requirements of modern CubeSats while offering enhanced performance and reliability.

The MIMO capability supports high data rates, catering to data-intensive applications, such as Earth observations, scientific experiments, or inter-satellite networking, where rapid and voluminous data transfer is essential. The proposed antenna's beamsteering ability was obtained without any electrical and mechanical sophistication in the entire antenna system, improving the CubeSat to ground station communication. By having characteristics such as a low profile and high gain and efficiency, the proposed leaky-wave antenna can also be a reliable candidate in a harsh environment, like space, especially for the next generation of CubeSat communications. Furthermore, having a CP feature can degrade the signal interference between the CubeSats.

After giving a thorough introduction and explaining the state of the art in Section 1, the detailed design of the proposed antenna is given in Section 2, followed by the results in Section 3. Finally, Section 4 offers the conclusions of this work.

2. Antenna Design and Configurations

This section details the design process and arrangement of the antenna. The suggested MIMO LWA was first developed for targeted frequency ranges before being incorporated into a 1U CubeSat with additional cavity layers. The radiation properties of the single-port design were analyzed and then adapted for a dual-port configuration. Performance enhancements, including the impedance bandwidth and isolation, are achieved by engraving nested U-shaped, T-shaped, and S-shaped slots onto the patches and using them as a neutralization system. Furthermore, the antenna's multilayered, stacked construction boosts its gain and radiation efficiency. The nested slots applied to the patches and the space between them reduce unwanted backside and end-fire radiation by leveraging the combined influence of transverse and longitudinal slots, resulting in a broadside radiation pattern that differs from traditional leaky-wave designs. A traditional leaky-wave antenna typically offers end-fire and back-fire radiation patterns, which are not particularly interesting or valuable for CubeSat communication applications, as the metallic walls of the CubeSat may cancel them. Therefore, in our proposed design, we have attempted to make the antenna radiate toward the broadside and outward from the antenna, as well as from the antenna to the CubeSat wall [30].

Figure 1 illustrates the perspective and side views of the proposed antenna before it is integrated into the CubeSat. As illustrated in Figure 1a, the proposed LWA is composed of six layers, each with specific heights (h_1, h_2, h_3, h_4, h_5, and h_6) and dialectic constants (ε_1 = 10.8, air (ε_2= 1), ε_3 = 2.08, ε_4 = 3.66, ε_5 = 3.66, and ε_6 = 11.2), which will be detailed in the following subsection.
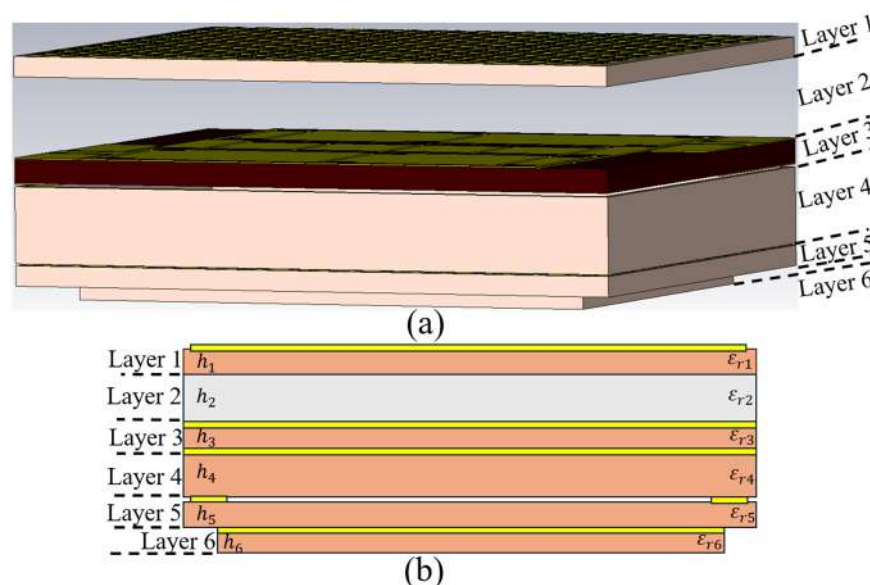
Figure 1. The proposed antenna: (**a**) perspective view and (**b**) side view.

Design Principles, Methods, and Techniques

Figure 2 depicts the individual layers of the suggested dual-port MIMO antenna. The development begins with a single-port configuration, subsequently upgraded to incorporate dual ports. The suggested MIMO LWA utilizes a rectangular patch connected to a transmission line, where one side serves as the input source, and the other is terminated in a 50 Ω load. The first phase involves applying fundamental formulas from Ref. [31] to determine the measurements of the rectangular patch and transmission line, thereby customizing the antenna for optimal functionality at 3.8 GHz (with $\lambda_0/2 < 39$ mm). Not all these well-established equations are not presented in this context and only a few are given here (Equations (1)–(3).

$$W = {}^{c}\!/_{2f_0\sqrt{\frac{(\varepsilon_r+1)}{2}}}, \ \varepsilon_{eff} = {}^{(\varepsilon_r+1)}\!/_2 + {}^{(\varepsilon_r-1)}\!/_2 \left(\sqrt{\left(1 + \left(\frac{12h}{w}\right)\right)} \right) \tag{1}$$

$$\Delta L = 0.412\,\mathrm{h}\frac{\left(\varepsilon_{eff} + 0.3\right)\left(\frac{w}{h} + 0.264\right)}{\left(\varepsilon_{eff} - 0.258\right)\left(\frac{w}{h} + 0.8\right)}, L_{eff} = {}^{c}\!/_{2f_0\sqrt{\varepsilon_{reff}}}, \ \mathrm{L} = L_{eff} - 2\Delta, \ L_g = L + (6h) \tag{2}$$

$$W_g = W + (6h) \tag{3}$$

After considering all the principles and equations of conventional and leaky-wave antennas, it should be noted that altering the antenna dimension to a larger and smaller size can shift the band to lower and higher bands. The leaky-wave configuration prioritizes strong directivity, a high gain, a low loss, and a simple structure. LWAs are classified as traveling-wave antennas, characterized by a wave propagating along an elongated framework regarding the wavelength. This feature generates currents along the antenna's length, leading to end-fire and back-fire radiation patterns influenced by the open-stopband (OSB) effect, as noted in Refs. [32,33]. They can be accurately represented by composite right-/left-handed (CRLH) transmission lines, integrating the properties of capacitors and inductors, and additional modifications are required to achieve a broadside radiation pattern. The proposed MIMO LWA integrates uneven components, such as lengthwise slots designed to enhance OSB performance and crosswise slots intended to address OSB-related challenges. As a result, these features adjust the radiation pattern to optimize it for broadside emission rather than end-fire or back-fire directions. Additionally, the slots

enhance the separation between antennas in the array and reduce surface waves generated by LWAs. The characteristic mode approach is utilized to study and develop these slots, assessing their influence on the radiation pattern throughout the design process—from start to finish—while accounting for the concepts of asymmetrical radiation, as shown in Figure 2.
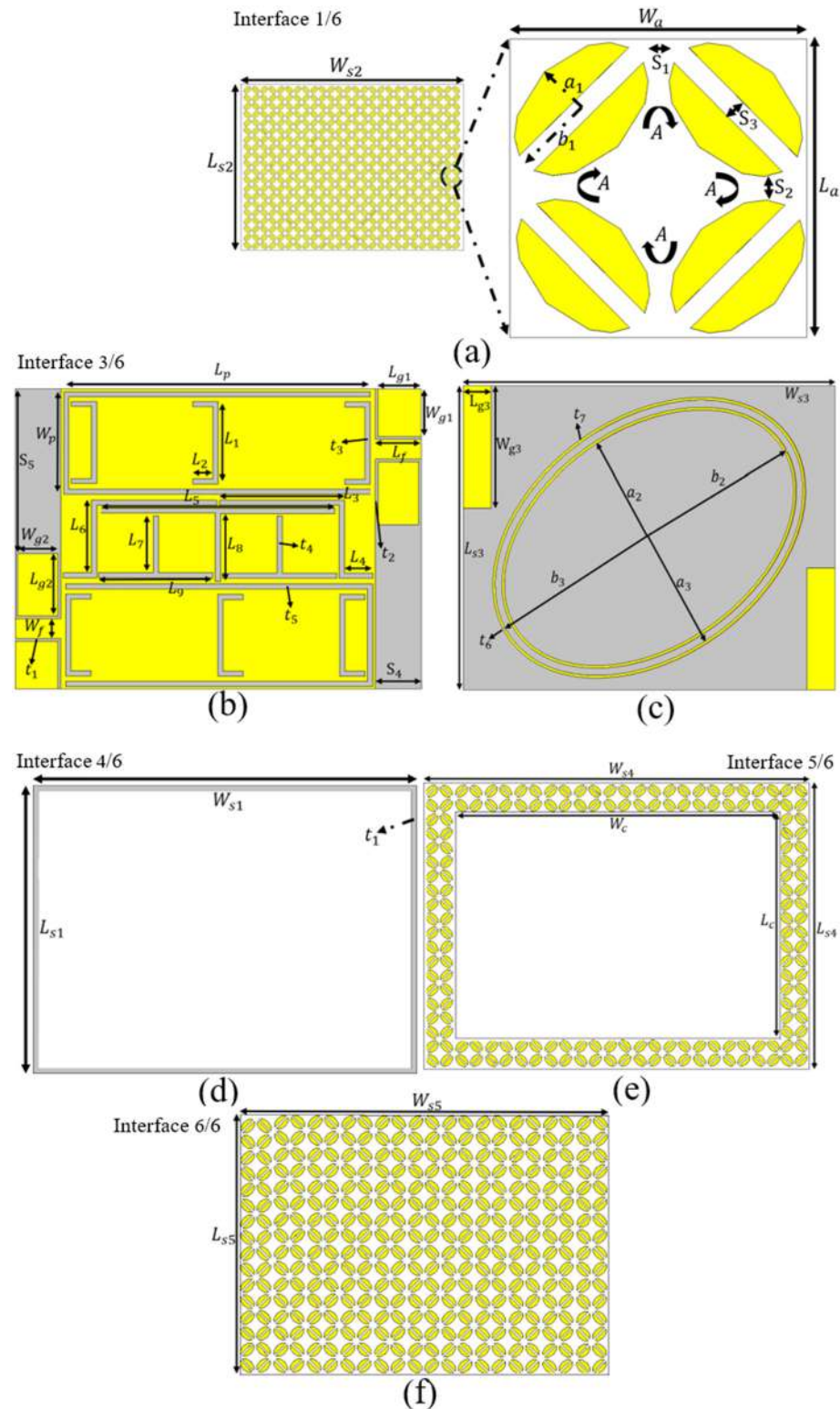

Figure 2. A simulated prototype of the proposed antenna: (**a**) layer 1 (Interface 2/6 is air), (**b**,**c**) layer 3, (**d**) layer 4, (**e**) layer 5, and (**f**) layer 6.

The waveguide port in the proposed antenna uses the TE_{10} mode, unlike the TE_{01} mode in the dielectric inset. As shown in this figure, the antenna's radiation relies on an asymmetrical structure to improve the OSB. The symmetrical slots with the TE_{10} mode produce no horizontal field at the aperture. In contrast, asymmetrical T- and L-shaped slots induce a horizontal TEM wave for broadside radiation. Adjusting slot asymmetries controls the TE_{10} leakage rate, and the new design mitigates leakage through slot spacing and asymmetries, maintaining fixed inset spacing [34].

The antenna initially utilizes basic microstrip lines (Interface 3/6) on a dielectric base and the ground coplanar waveguide technique, where waves travel through the rectangular patch and escape whenever they encounter a slot in the design. The currents originating from the source flow through the microstrip, scattering due to impedance variations on the surface to form the intended radiation. The antenna achieves two resonances at 3.2 GHz and near 7.6 GHz. Moving to the second phase, a rectangular patch is modified by carving out a long longitudinal U-shaped slot, introducing a disturbance and leakage. This disruption in the patch's current flow boosts the array's beamwidth and impedance range while generating an additional resonance around 5.6 GHz and expanding the upper 7.6 GHz band. However, this adjustment pushes the operational frequencies—3.2 GHz, 5.6 GHz, and 7.6 GHz—upward, needing a shorter transverse section in the U-slot to counteract the shift. The transverse slot acts as a left-handed capacitive series, altering the radiation direction away from both end-fire and back-fire patterns. In the third stage, three smaller U-shaped slots of varying widths were placed in a nesting configuration, taking into account the surface current distribution (SCD) figures presented later in the text. These slots offer a multi-band feature that introduces an approximate extension at a lower band, from 3.8 GHz, and a resonance around 8.65 GHz. It also widens the lowest resonance and slightly lowers the third one. In the fourth stage (Figure 3), two strips were added at the back of the substrate as the ground section of the ground co-planar waveguide (GCPW) technique to broaden the operational bandwidths at these bands, along with another resonance around 15 GHz. In addition to these ground strips, two elliptical split ring resonators (ESRRs) forming a complementary ESRR (CESRR) are added at the back, covering the substrate radially to reduce the negative fringing fields and improve the antenna's performance around 8.5 GHz. The CESRR, also known as a sub-wavelength resonant structure, creates a redistribution in current and also electromagnetic coupling effects, which affect the impedance matching positively and can result in a wider BW around the X band. It also functions as an artificial magnetic conductor (AMC)-like structure, which can degrade the surface wave propagation as well as the back radiation, resulting in a higher gain. Moreover, the surface wave reduction also surpasses the ohmic loss, offering improvements in radiation efficiency.
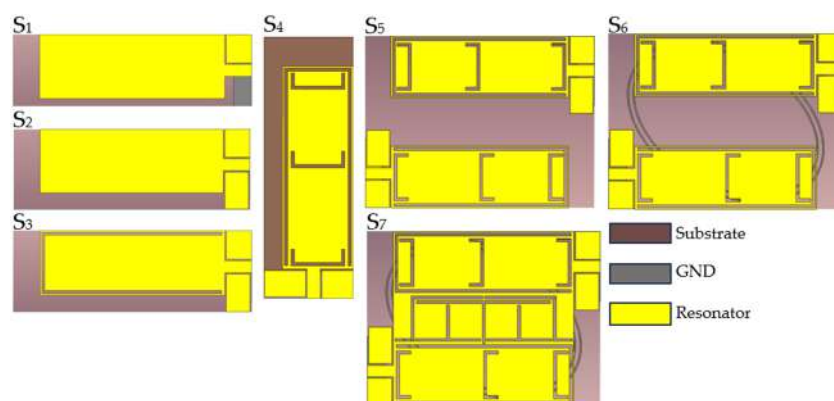

Figure 3. The designed stages of layer 3 (Interface 3/6) from stage 1 to stage 7 (S_1–S_7).

After obtaining the required resonances and resonance modes, it was time to enhance the antenna's performance while maintaining miniaturized dimensions, as this is one of the primary objectives of the antenna for CubeSat communications. It should be noted that the one-port antenna was extended to a two-port MIMO antenna and fed inversely and longitudinally with a 180-degree rotation. Initially, a copper strip connected the two ports, adding another resonance at the higher band, around 22 GHz. However, the impedance bandwidth was reduced at the lower and middle bands. The radiation efficiency was diminished due to surface wave increments after adding this strip and so was the increment in mutual coupling. Therefore, a neutralization network consisting of nested S-shaped and T-shaped slots was etched from this strip. These slots improved the OSB and isolation between the ports (Figure 4).
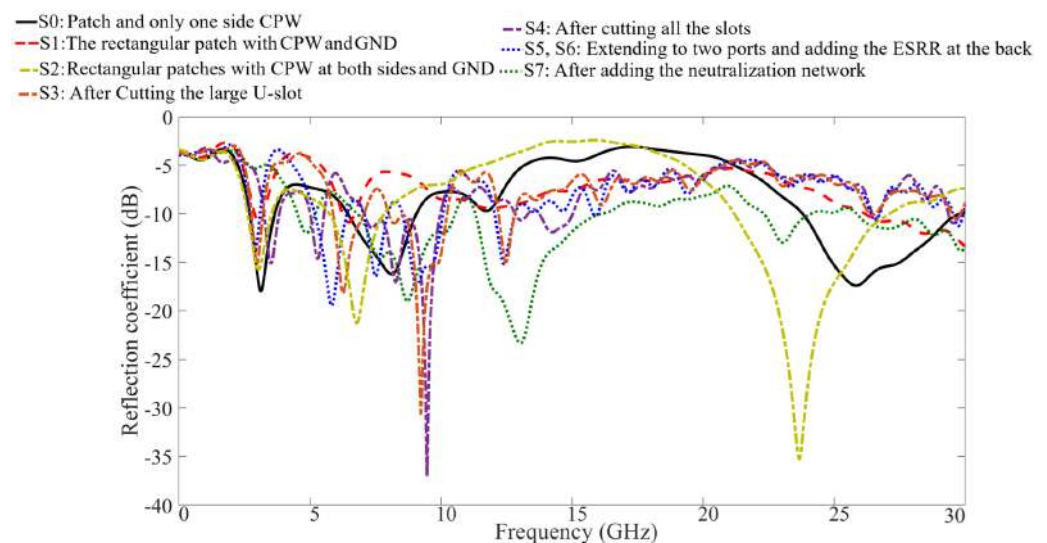

Figure 4. The reflection coefficient results of each stage of layer 3 (Interface 3/6).

Figure 5 shows the proposed antenna's SCD for each working band. It shows that the antenna's current density peaks around the transmission line and CPW feeding. By increasing the mode and frequency to 5.6 GHz, the SCD extends and reaches its maximum near the large U-shaped slot, reducing as it approaches the end of the patch. This pattern holds for the SCD in the subsequent frequencies and resonant modes, as illustrated in Figure 5c,d, where the highest concentration is observed around the large U-shaped slot and in the proximity of the small U-shaped slots. In addition, Figure 5e,f depict the higher resonance and modes of the SCD and the optimized associated location for them, which should be considered during the design process and when etching them.
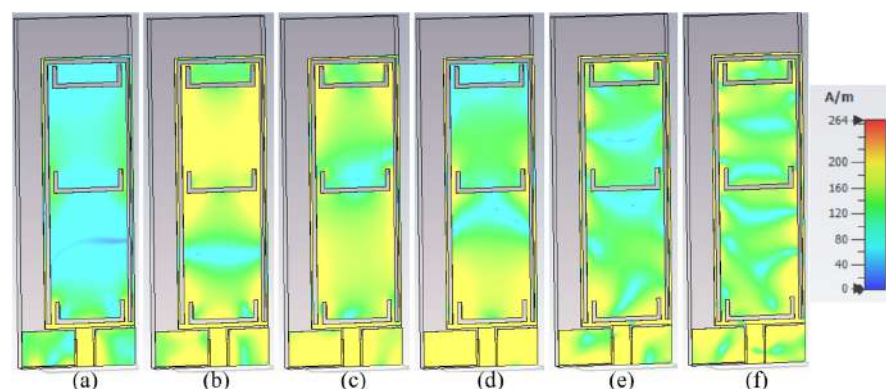

Figure 5. SCD for a single element at (**a**) 3.8 GHz, (**b**) 5.6 GHz, (**c**) 7 GHz, (**d**) 9 GHz, (**e**) 22 GHz, and (**f**) 28 GHz.

To understand the structure of the antenna and how it functioned during the design procedures, a parametric study was performed, and each parameter was optimized accordingly. For instance, parameters like the patch dimensions—specifically, the patch length (L_p) and width (W_p)—the length of the rear ground plane (L_{g3}), and the length of the central S-shaped slot (L3) could significantly affect the antenna's impedance matching and working bands. Following this, varying the patch length directly affects the antenna's fundamental resonant frequency, as increasing L_p extends the effective electrical length of the current path, resulting in a lower resonant frequency due to the inverse relationship between resonant frequency and effective length and vice versa. Nevertheless, the coupling effect between the patch and them created some undesired ripples. On the other hand, the width of the patch affected the BW around every resonance, as a wider one enhances the desired BW, and a reduction in that also makes the BW narrower. L_3 also showed some significant changes in BW, especially around the first resonance, by creating some discontinuity in the current passing around it. L_{g3} can also play a crucial role in controlling the lower-frequency bandwidth, as its increment beyond 3 mm adversely affects the impedance matching in the lower frequency band by modifying the ground's reflection phase. A longer ground causes destructive interference at specific frequencies, reducing efficiency and the bandwidth. On the other hand, lowering it improves coupling between the radiating patch and the substrate, improving the BW around the first and third resonances. The optimized dimensions of the antenna, as determined by a parametric study, are presented in Table 2. It should be mentioned that the optimization process was performed using Computer Simulation Technology (CST) studio suite and the choice of the genetic algorithm in the CST itself.

Table 2. The proposed antenna's structural parameters.

Parameters	Values (mm)	Parameters	Values (mm)	Parameters	Values (mm)	Parameters	Values (mm)
W_{s1}	40.00	A	45°	L_{s3}	30.00	b_3	18.00
L_{s1}	30.00	S_1	0.25	L_{g3}	3.00	L_p	31.00
t_1	0.25	S_2	0.30	W_{g3}	12.00	L_{g1}	4.25
W_{s2}	40.00	S_3	0.20	t_7	0.25	W_{g1}	4.75
L_{s2}	30.00	a_1	0.50	a_2	11.00	L_f	4.50
W_a	3.00	b_1	0.75	a_3	12.00	W_p	10.50
L_a	3.00	W_{s3}	40.00	b_2	17.00	t_3	0.50
L_1	8.20	L_{g2}	6.25	L_6	7.40	L_8	6.85
L_2	2.00	W_{g2}	4.00	L_7	5.75	t_4	0.50
S_5	16.50	W_f	2.00	L_5	23.00	L_3	12.25
L_4	2.75	t_2	0.25	t_5	0.50	S_4	4.50
W_{s4}	40.00	L_{s4}	30.00	W_c	34	L_c	23.75
W_{s5}	34	L_{s5}	24	h_1	1.28	h_2	5.00
h_3	1.50	h_4	4.80	h_5	1.28	h_6	1.00
L_9	11.25	t_6	0.25				

Following a brief analysis of some of the antenna's parameters in Interface 3/6 and their optimization, the S-parameter outcomes were evaluated at each phase of incorporating additional layers into the antenna. Figure 6 illustrates the reflection and transmission coefficient results after adding each layer (adding layers 1, 2, and 4–6). It reveals that the three resonance modes and corresponding bands are achieved around 3.8 GHz, 7.5 GHz, and 22 GHz in the absence of slots and a ground plane on the back, and after cutting the slots, the BW was enhanced around 8 GHz. Moreover, adding a ground and the CESRR at the back shifted the whole band to a higher band, and another band was created around 12 GHz. Adding layer 1 (Interface 1/6) of a MTS, as shown in Figure 2a, enhances

the impedance bandwidth and radiation performance, such as gains and efficiency. It should be mentioned that coffee bean MTSs are so named due to their resemblance to coffee bean shapes, and they are a specialized type of MTS, characterized by their unique geometry, looking like an elliptical curve with a slot at the middle. These structures are utilized to manipulate electromagnetic (EM) waves with high precision, offering distinct advantages over traditional antenna designs. They can tailor electromagnetic responses, such as controlling the polarization and phase. Their design enables subwavelength-scale structures, allowing for compact and lightweight antennas (not too strict, based on the $\lambda/2$ rules). They can control the phase, amplitude, and polarization of EM waves through the arrangement and orientation of their unit cells. They can also support dual or multi-resonant points, facilitating wideband performance (e.g., 13–20 GHz or 14–25 GHz in some designs) suitable for multi-band applications. In addition, they have the ability to convert from LP to CP. Considering all these features, four unit cells make an array of a flower-like structure formed by rotating the cells by 45 degrees. Their elliptical shape, slot geometry, and their rotation create a symmetric phase gradient control that enhances constructive radiation toward the broadside direction, resulting in higher directivity and gains as compared to square or circular shapes. This structure also minimizes the side lobes and focuses energy on the main lobe [35].
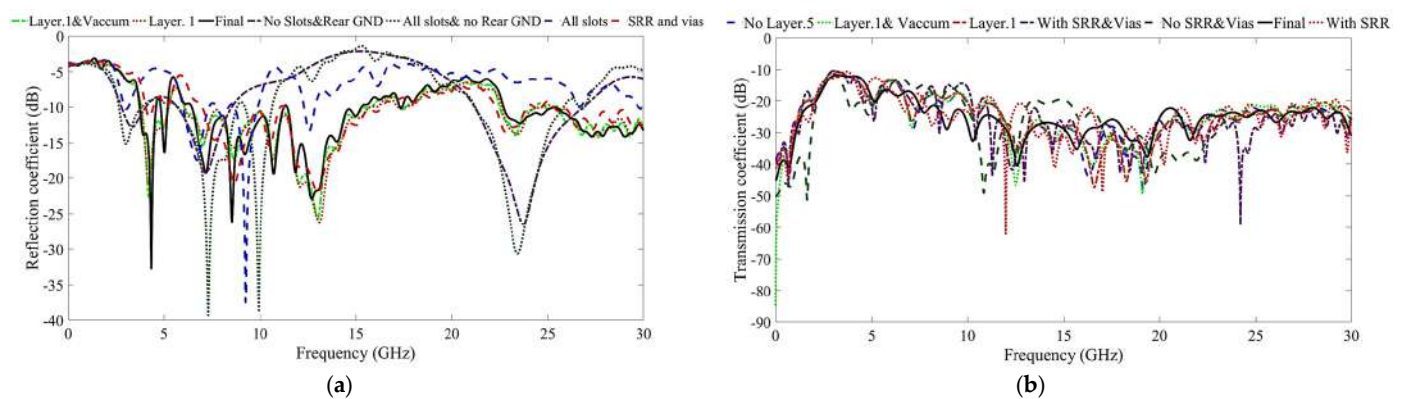

Figure 6. The reflection (**a**) and transmission (**b**) coefficient results of the proposed antenna after adding each layer of the antenna at each stage of the design.

A layer of air with a thickness of 5.4 mm (layer 2, as Interface 2/6 is not depicted in Figure 2) exists between layer 1 and layer 3 to further enhance the gain and efficiency. It should be noted that, considering electromagnetic wave theories, this air gap (with relative permittivity close to 1) acts as a transitional medium that minimizes the impedance mismatch between the antenna substrate and free space, improving the impedance BW and working BW. It also preserves the phase velocity of radiated waves and decreases possible power dissipation through substrate losses so that higher radiation efficiency can be achieved by directing more energy into free space rather than being absorbed or trapped within the structure. Moreover, it provides more effective excitation and directional control of the leaky modes, contributing to efficient beamsteering. In terms of polarization, the layer of air can reduce the AR effectively by making a balance between the phase and amplitudes of the modes orthogonally. It also suppresses the surface waves created by substrate loss modes, enhancing the radiation efficiency. Afterward, the antenna was stacked with a layer of cavity (Interface 4/6), followed by a rectangular ring layer with coffee bean arrays on it (Interface 5/6) and an MTS layer (Interface 6/6). It should be mentioned that Interface 6/6 has a smaller dimension using MTS arrays that are identical to those in Interface 1/6 and Interface 5/6. The cavity layer has almost the same effect as the air layer, with more impact on suppressing the back radiation and side lobes and

sharpening the radiation pattern towards the desired radiation constructively, since it is confined by thin layers of substrate used for layer 3. Interface 5/6 introduces a periodic subwavelength structure that acts as a frequency-selective surface (FSS) element, creating passbands and stopbands in order to enhance the bandwidth around the desired working bands. The ring structure further confines the electric field positively in proximity to the leaky-wave aperture. Last but not least, Interface 6/6, with smaller dimensions and having the same MTS arrays as layer 1, creates further phase tapering spatially by acting like a nearfield phase correcting structure and also suppresses the grating lobes towards the undesired direction. Figure 6 also illustrates the transmission coefficient results for the antenna with each layer added, as well as the stages of antenna performance improvement. It shows that cutting the slots from the patch and adding layer 1 and the vacuum layer enhanced the isolation, especially at higher bands. It provides the entire band with an isolation of more than 13 dB. After assessing and evaluating the S-parameter results for the antenna, its radiation efficiency and gains should be enhanced, keeping in mind that miniaturization is also vital for CubeSat.

Considering the S-parameter results of the antenna after adding each layer, the absorption coefficient, an important factor in utilizing MTS structures, was calculated using Equation (4):

$$A(f) = 1 - |S_{11}(f)|^2 - |S_{21}(f)|^2 \qquad (4)$$

It defines a "perfect absorber" when $A(f) > 99\%$ (i.e., absorption coefficient ≈ 1.0). It shows that this can be achieved when both reflection and transmission are minimized through impedance matching and resonant loss mechanisms [36]. For practical RF energy harvesting, absorption values above 70–80% are considered excellent, while 60% and above is workable when compensated by matching circuits and rectifier efficiency. Multi-band metamaterial absorbers are often designed to achieve >80% absorption at multiple discrete frequencies, and >60% across broader bands are acceptable, especially when balancing design trade-offs [37]. Considering all this information, the proposed antenna provides a quantitative measure of the amount of incident RF power absorbed by the structure. The resulting absorption spectrum is shown in Figure 7. As shown, the structure achieves a peak absorption of 0.85 at 7 GHz. The absorption is between 0.6 and 0.8 across the working bands, which meets typical performance expectations for energy-harvesting MTSs and broadband applications.
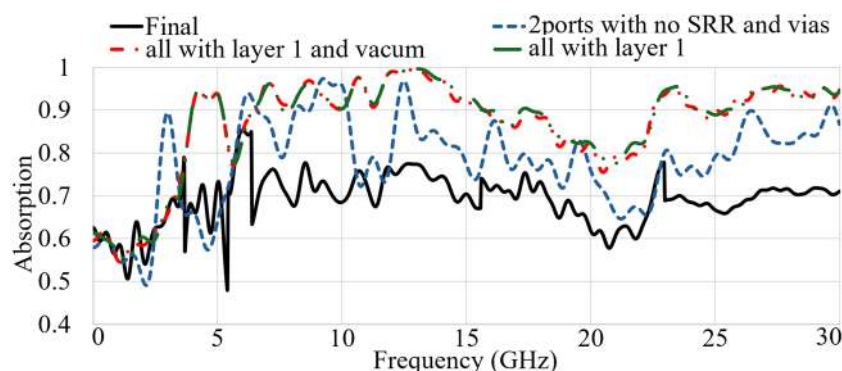

Figure 7. The absorption coefficient of the proposed antenna.

3. Results and Discussion

3.1. Simulation and Measured Evaluations in Free Space

This section details the simulation and measurement outcomes for the proposed antenna, both standalone and integrated with a CubeSat. Figure 8 illustrates the experimental setup for testing the antenna in free space alongside the constructed antenna prototype used

to verify theoretical and simulated findings. The antenna's S-parameters were evaluated using a Keysight (formerly HP/Agilent) 8722ES Vector Network Analyzer (VNA), which operates over a frequency range of 50 MHz to 40 GHz. The VNA was configured with a frequency sweep tailored to the antenna's operational bands, featuring 201 data points per sweep and an intermediate frequency (IF) bandwidth of 10 kHz, which balances resolution and noise. Before measurements, a full two-port calibration was performed using a precision SOLT (Short-Open-Load-Thru) calibration kit, with the reference plane established at the end of the coaxial cable, directly at the SMA connector interfacing with the antenna. This ensured accurate de-embedding of cable losses and connector mismatches. High-quality, phase-stable RF cables were used, and ferrite chokes were applied to suppress common-mode currents. The antenna was mounted on a 1U copper CubeSat mock-up platform to simulate realistic in-satellite mounting conditions, accounting for any possible coupling or detuning that may occur due to platform integration. Radiation pattern measurements were conducted in a fully anechoic chamber designed to suppress unwanted reflections and external electromagnetic interference. The antenna under test (AUT) was placed on a motorized turntable mounted on a non-reflective support at a height corresponding to the antenna's phase center. The measurements were performed in the far-field region, with a separation distance of 3 m between the AUT and a dual-polarized standard gain horn antenna, which served as both the transmitter and receiver. The chamber was equipped with RF absorbers rated for operation up to 40 GHz to minimize wall reflections. Patterns were captured in both the E-plane and H-plane, and both co- and cross-polarization components were recorded. The angular resolution of the turntable sweep was set to 5° increments over the range of 0° to 360° in azimuth, with elevation angles adjusted manually as needed. Polarization alignment was carefully verified to ensure accurate measurements of intended field components. All measurements were repeated multiple times to confirm repeatability, and system errors, such as multipath, connector instability, or ambient noise, were monitored and minimized through background measurements and time gating.
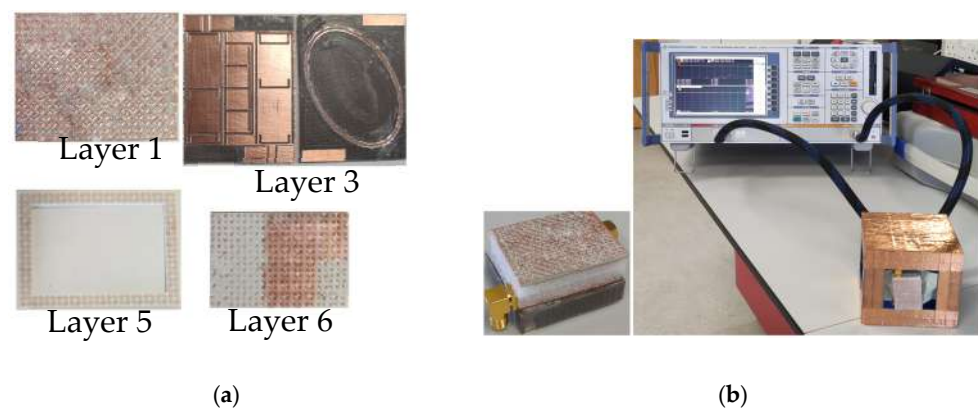

Figure 8. (**a**) Fabricated layers of the antenna and (**b**) testing the designed antennas in open-air and CubeSat environments.

Figure 9 depicts the simulated and experimental reflection and transmission coefficient results of the proposed antenna, with good agreement and little discrepancy between them. Minor discrepancies occurred, because the conditions and environment considered during the simulation were ideal unlike those during the measurements. For instance, the ports in the simulation were waveguide ports unlike the measurements, which were actual high-frequency SMA ports. In addition, several fabrication tolerances might have occurred, such as minor misalignments between the MTS layer and other layers when gluing them together, which might have changed the thickness and space among them slightly. Additionally, during the measurements, connector losses, soldering imperfections,

and calibration limitations (e.g., probe placement accuracy or port matching) could have contributed to deviations in S21. Moreover, in our setup, the presence of measurement cables and fixtures—which are not included in simulations—can unintentionally couple to the antenna or introduce parasitic effects, especially in compact or high-frequency designs. Apart from a bit of discrepancy, a consistent tendency in the working BW and isolation occurred between their simulated and measured outcomes. Nevertheless, the measurement was repeated until less discrepancy was observed. Before evaluating the antenna's radiation pattern for both the simulation and measurement assessment, it was important to investigate the antenna's beamsteering and directions [38].
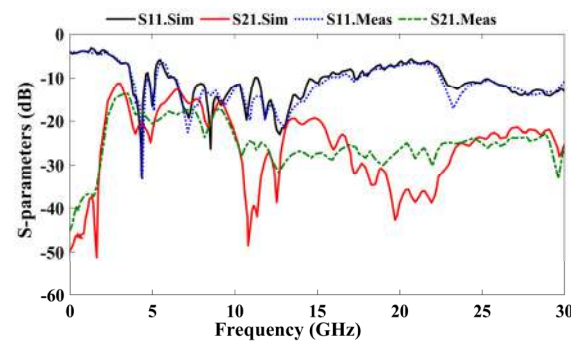

Figure 9. The simulated and experimentally obtained S-parameter data for the designed antenna in an open environment.

These bands are not independently switched or isolated via filtering; instead, the antenna maintains continuous, wideband impedance matching and radiation performance across all three bands. It also shows that the antenna can offer a wideband behavior and also stable radiation characteristics, like directive gains, efficiency, and lower levels of sidelobes at working BWs. However, a simultaneous multi-band operation (e.g., transmitting in one band while receiving in another) would require the integration of multi-band RF front-end circuitry or filtering at the system level to prevent mutual interference and ensure signal separation. The antenna's beamsteering capability is depicted in Figure 10, where ports 1 and 2 are active separately. It shows that the antenna can steer the beams of 18°–55° and 206°–341° when port 1 (Figure 10a) and port 2 (Figure 10b) are active, respectively.
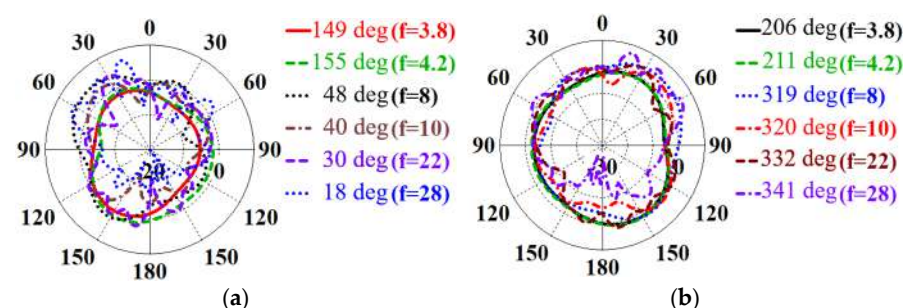

Figure 10. A simulated evaluation of the beamsteering capability of the proposed antenna (**a**) Port 1 is active and (**b**) Port 2 is active.

After verifying the simulated and measured S-parameters of the antennas and confirming their perfect agreement, the antenna's radiation pattern was measured to demonstrate that it radiates properly and matches the simulated radiation pattern. Figure 11 depicts the simulated and measured radiation patterns of the E and H fields at the desired frequency bands. Perfect agreement is depicted between the simulated and measured E and H field patterns. It also shows that they are bidirectional at lower bands and become more directional at higher bands.
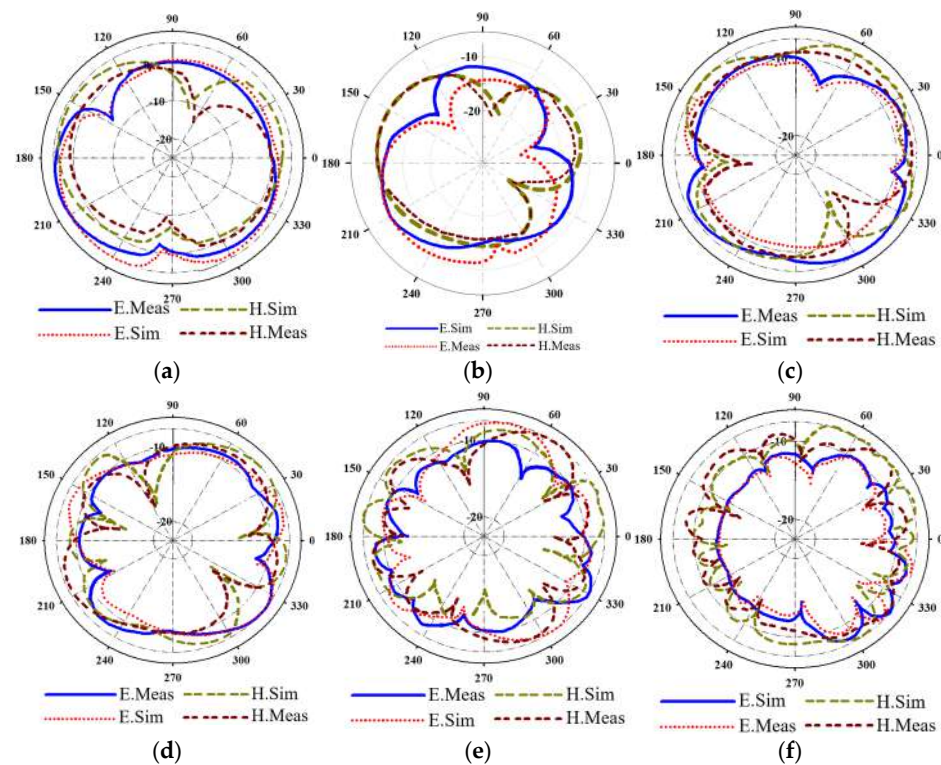
Figure 11. The simulated and measured radiation patterns of the antenna's electric and magnetic fields in free space at (**a**) 3.8 GHz, (**b**) 5.2 GHz, (**c**) 8 GHz, (**d**) 10 GHz, (**e**) 24 GHz, and (**f**) 28 GHz.

3.2. Simulation and Measured Evaluations Integrated with CubeSat

Figure 12 illustrates the full-wave simulation setup of a 1U CubeSat integrated with four arrays of the proposed MTS-based leaky-wave MIMO antenna. The CubeSat structure is modeled with copper walls to accurately represent the conductive boundaries typically used in real satellite platforms, accounting for possible reflections and mutual coupling effects during electromagnetic simulation. The antenna arrays are strategically mounted on four lateral faces of the CubeSat to provide nearly omnidirectional spatial coverage in the azimuthal plane. This configuration enables robust link availability with ground stations or other satellites, regardless of the CubeSat's orientation in low Earth orbit. The integration setup was designed to study the radiation performance, mutual coupling between elements, and the effects of CubeSat's metallic enclosure on the antenna's behavior. The cavity-backed design and spacing from the CubeSat body also help minimize surface currents and enhance directional gains. By simulating this realistic deployment scenario, we ensure the proposed antenna maintains its high gain, wideband performance, and beamsteering capabilities even when installed on the satellite, which is critical for validating its suitability for practical CubeSat communication missions.

Figure 13 presents the simulated S-parameters—specifically, the reflection (S11) and transmission (S21, S31, etc.) coefficients—of the proposed antenna when integrated into a 1U CubeSat platform. The reasonable effects of the metallic and copper walls of the CubeSat on impedance matching and working BWs are observed in Figure 13. These effects can be seen by the created stopbands in the simulated band, which might have been produced by the mutual coupling created after locating the antennas that interacted with the CubeSat. Nevertheless, the antenna maintains effective operation across the target frequency bands (3.75–5.25 GHz, 6.4–15.4 GHz, and 22.5–30 GHz), confirming its robustness in a realistic satellite environment. Figure 13 also illustrates the transmission coefficients between ports located on different antenna arrays. The results demonstrate excellent port-to-port isolation, particularly between port 1 on array 1 and all other ports. The transmission coefficients

consistently remain below –15 dB across the operating bands, indicating minimal mutual coupling. Having a high degree of isolation among the antenna arrays' ports is vital, because this assures signal loss reduction and independence between the ports, which enhances the channel capacity and allows for a high data rate. This also proves that it is suitable for MIMO communications, showing minimum interference.
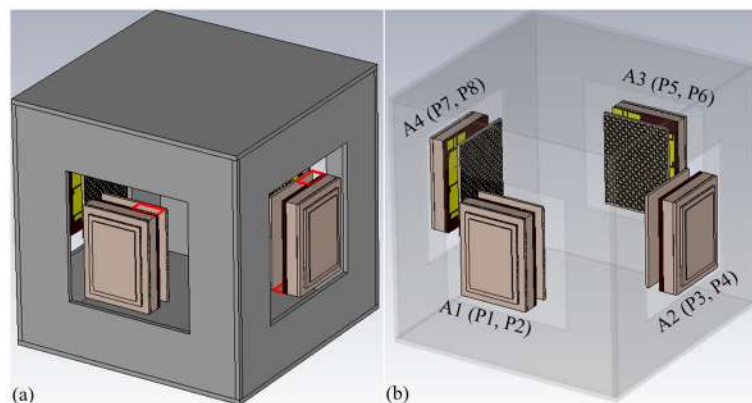

Figure 12. Simulation setup of the proposed antenna arrays in CubeSat: (**a**) the CubeSat and the arrays and (**b**) antenna arrays.
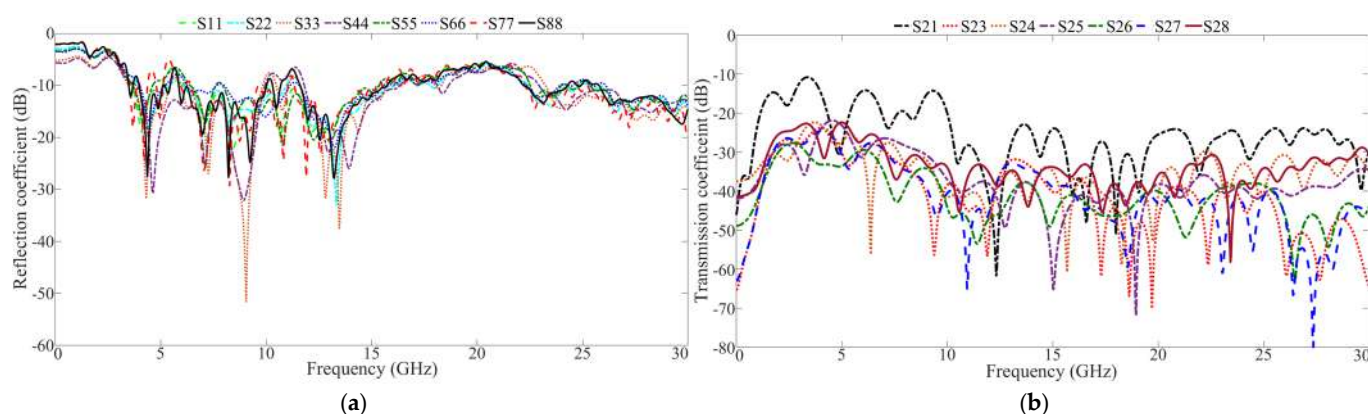

Figure 13. The reflection (**a**) and transmission (**b**) coefficient results of the proposed antenna arrays in CubeSat.

The simulated radiation patterns of the proposed antenna for arrays A1 and A2, when they are integrated with the CubeSat, are presented in Figure 14. This figure also depicts how these arrays behave at the working bands and that the radiation pattern is all directed outward from the CubeSat. Therefore, the proposed antenna arrays can have a wide-ranging spatial coverage, improving communication links even with different orientations. It should be mentioned that this assessment was carried out considering far-field principles during the simulations (the red lines are the radiation, the light blue is the 3 dB beamwidth, and dark blue line is the main direction).

After evaluating the radiation pattern and far-field characteristics, like directivity, gain, and efficiency, this antenna array in CubeSat offered a 3 dB beamwidth of up to $28.8°$. In addition, the sidelobe levels (SLLs) were also calculated, offering -14.1 dB and -10.5 dB for full array integration and individual arrays, respectively. This suppressed SLL also decreases the level of interference and enhances radiation efficiency. These characteristics confirm the antenna's effectiveness in space-constrained, high-performance CubeSat platforms. To demonstrate the stability of circular polarization under beamsteering, we evaluated the axial ratio (AR) at multiple steering angles across each operating band.

The results, shown in Figure 15, confirm that the AR remains below 3 dB within the main beam direction for all relevant scan angles and frequency ranges. This verifies that the antenna maintains consistent CP performance across its operational bandwidth and beamsteering range, which is essential for preserving polarization alignment and reducing polarization mismatch losses in CubeSat communication links.
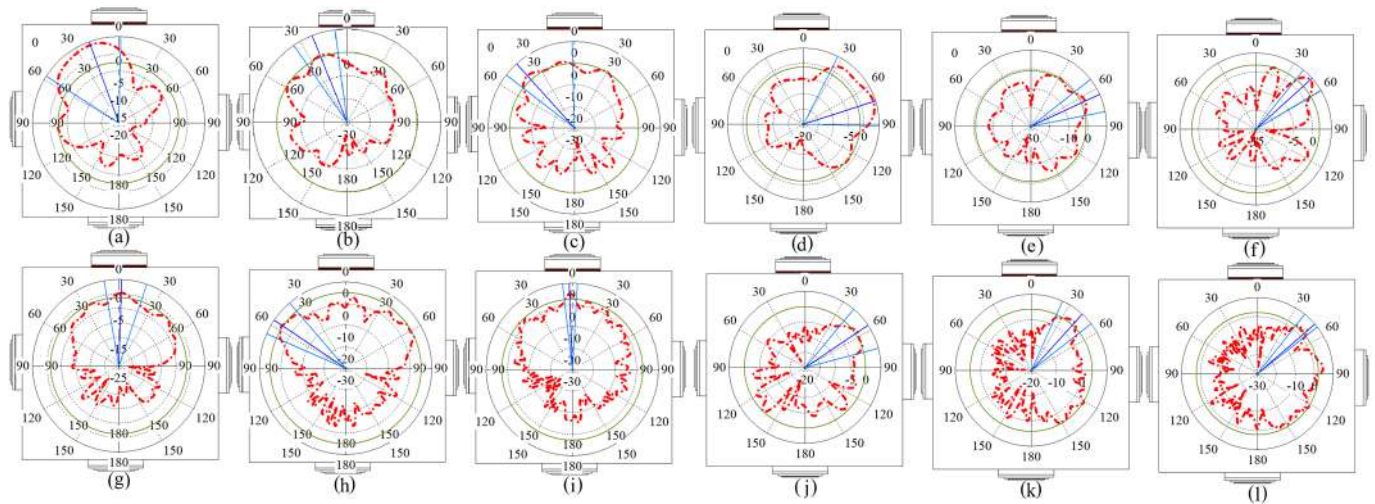

Figure 14. The radiation pattern of the antenna in CubeSat with port 1 (P_1) in array 1 (A_1) at (**a**) 3.8 GHz, (**b**) 5.8 GHz, (**c**) 8 GHz, (**g**) 10 GHz, (**h**) 22 GHz, and (**i**) 28 GHz and port 7 (P_7) in array 2 (A_2) at (**d**) 3.8 GHz, (**e**) 5.8 GHz, (**f**) 8 GHz, (**j**) 10 GHz, (**k**) 22 GHz, and (**l**) 28 GHz.
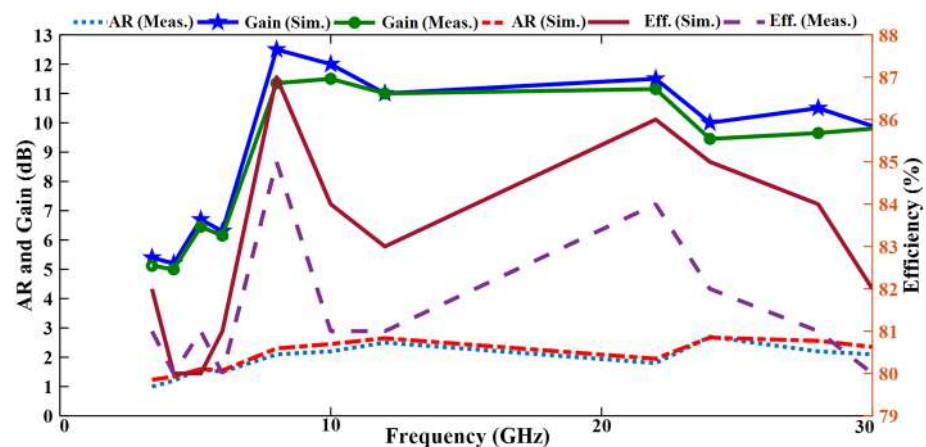

Figure 15. The simulated and measured axial ratio, gain, and radiation efficiency results of the proposed antenna.

The proposed antenna, as shown in Table 3, demonstrates significant improvements over previous studies in terms of compactness, frequency coverage, gain, and multifunctionality. This table also shows that the proposed antenna can outperform almost all the works presented in Table 3, even with its low profile of 40×30 mm^2, especially designed for 1U CubeSat communications. It also offers multi-band operation across three distinct frequency ranges (6.4, 15.4, and 22.5–30 GHz), making it highly suitable for multifunctional CubeSat missions, including inter-satellite links, payload telemetry, and RF sensing. Unlike several references that lack the beamsteering capability or that operate in narrow bands, our design integrates MTS and leaky-wave antenna (LWA) principles, enabling beamsteering from 18° to 155° (Port 1) and 206° to 341° (Port 2)—a wide angular range rarely achieved in such compact formats. While works like [39,40] offer high gains (20–29 dBi), they demand significantly larger footprints (e.g., 100×200 mm^2) and some support only

single-band or limited functionality. Additionally, our design achieves a commendable gain of 12.9 dBi and 85% radiation efficiency, positioning it ahead of most designs with incomplete efficiency data or values < 80% (e.g., [41]). Moreover, the use of circular polarization (CP) ensures robustness in orientation-sensitive CubeSat links, a feature shared with only a few high-performing systems [39,42]. Overall, our work combines miniaturization, beam agility, high gains, and CP support, making it one of the most balanced and CubeSat-ready antenna solutions to date. In addition, compared to the other antennas listed in Table 3, the proposed antenna occupies only 1200 mm^2, which is 81–99% smaller in printed area than most existing designs. For example, it achieves a 95.6% reduction in area compared to [25] (27,480 mm^2) and is 98.7% less than that of [41] (90,000 mm^2). Additionally, some designs (e.g., [40]) require integration into larger CubeSats (6U), while our compact structure fits efficiently within a 1U CubeSat, offering up to 83% reduction in spatial volume requirements.

Table 3. A comparison of the proposed antenna and several antennas designed for CubeSat communications.

Ref.	Size (mm^2)	fr (GHz)	Gain (dBi)	Eff (%)	Polarization	CubeSat Type	Beamsteering (°)	Improvement Techniques	Printed Area (mm^2)
[25]	120 × 229	9, 10	<10	<90	N/A	N/A	−75_75	SIW and Nyquist metasurface	27,480
[26]	<85 × 85	36.5–27	N/A	N/A	Dual	N/A	15_45	IRS and metasurface	7225
[43]	131 × 131	5.5	10.7	N/A	N/A	N/A	−48_48	Reconfigurable FSS	17,161
[28]	80 × 80	3.6	8	<80	N/A	N/A	−30_30	Partially reflecting surface	6400
[44]	21.3 × 21.3	8, 11.2	6.45, 5.34	N/A	Dual, CP	3U	N/A	Slot antenna	453.69
[45]	141 × 117	5.1	5.9	N/A	CP	1U	N/A	N/A	16,497
[42]	193 × 193	5.8	6.98	N/A	CP	1U	N/A	Transparent and glass antenna	37,249
[41]	<300 × 300	10	15	65	CP	1U	N/A	Fabry–Perot cavity	90,000
[39]	100 × 100	8.2	20	97.5	CP (RHCP)	1U	N/A	Unequal series with parallel power dividers	10,000
[40]	100 × 200	8.425	29.2	45	CP (RHCP)	6U	N/A	Offset-fed reflectarray	20,000
This work	40 × 30	3.75–5.25, 6.4–15.4, 22.5–30	12.9	85	CP	1U	Port1: 18_155 Port2: 206_341	LWA and MTS	1200

The achieved radiation efficiency of 85% in the proposed MTS-based leaky-wave MIMO antenna is the result of a carefully engineered design that minimizes typical loss mechanisms while maximizing electromagnetic performance. The antenna incorporates a flower-shaped MTS with coffee bean-like unit cells, which effectively manipulates surface currents and suppresses unwanted surface wave propagation. The inclusion of a cavity layer, rather than introducing an excessive loss, was optimized to enhance interlayer coupling and maintain impedance matching across the operating bands without degrading efficiency. Low-loss dielectric materials with carefully selected permittivity values were employed to minimize dielectric absorption, and high-conductivity metals were utilized for radiating elements to mitigate ohmic losses. The compact 40 × 30 mm^2 footprint further limits propagation losses and supports integration within CubeSat form factors. Full-wave simulations were conducted using realistic models in CST Microwave Studio (or HFSS),

incorporating dielectric loss tangents, conductor surface roughness, and proper meshing to emulate fabrication tolerances. These simulation parameters were chosen to ensure that the reported efficiency closely reflects practical performance. The antenna's high gain (12.5 dBi), wideband response across three frequency bands, and stable circular polarization all support the validity of this high-efficiency result. Collectively, these factors justify the reported 85% radiation efficiency and highlight the effectiveness of the proposed design for high-performance CubeSat communications.

The proposed MIMO leaky-wave antenna offers several features that lend themselves to future research. One research direction involves the use of beamsteering techniques such as reconfigurable MTSs, which provide dynamic control over the radiation pattern with no mechanical changes. This special function enhances the reliability of the communication link between the ground station and other satellites in LEO. Moreover, early discussions have been initiated with collaborators at the European Space Agency (ESA) to explore the potential for incorporating this antenna into next-generation CubeSat missions focused on inter-satellite networking and onboard autonomous communication routing. Further, the thermal and radiation resilience of the antenna materials under extended space exposure will be investigated through accelerated aging tests and radiation hardness evaluations. For higher power use cases beyond the 2 W range, the nonlinear performance and dielectric breakdown behavior of the MTS and substrate materials will be studied, particularly under pulsed power or prolonged high-duty-cycle operation. Lastly, the integration of this antenna with onboard energy-harvesting systems or intelligent beam-forming ICs will be explored to create a fully autonomous, compact, and adaptable CubeSat transceiver platform capable of supporting diverse missions from Earth observations to deep-space relays.

Beyond CubeSat applications, the compact footprint, high gain, and broadband capabilities of the proposed MTS-based leaky-wave MIMO antenna make it a strong candidate for adaptation to other space-constrained platforms, such as unmanned aerial vehicles (UAVs) and terrestrial Internet of Things (IoT) systems. For UAVs, where size, weight, and aerodynamic integration are critical, the antenna could be re-simulated using conformal or flexible substrates (e.g., polyimide or liquid crystal polymer) to integrate seamlessly with curved fuselage surfaces. Beamsteering features would enable dynamic tracking of ground control stations or mesh-connected UAVs. For terrestrial IoT deployments—especially those demanding long-range, directional, and high-throughput communication, such as smart agriculture, environmental monitoring, or infrastructure surveillance—the antenna could be retuned to operate efficiently in sub-6 GHz or unlicensed millimeter-wave bands (e.g., 5.8 GHz, 24 GHz, or 60 GHz) by adjusting the patch geometry and substrate dielectric profile. The low-power requirement, dual-port MIMO functionality, and polarization diversity further align with the energy and bandwidth constraints typical of IoT systems.

4. Conclusions

The novel miniaturized circular polarized dual-port MTS-based leaky-wave MIMO antenna presented in this study represents a significant advancement in CubeSat communication technology. It has a small size of 40×30 mm^2, operating at 3.75–5.25 GHz, 6.4–15.4 GHz, and 22.5–30 GHz, allowing it to meet the size limitations of CubeSats for space missions. It can also offer reliable long-distance communication, especially for LEO, with its limited-power condition, as it achieves a high gain and efficiency of 12.5 dBi and 85%, respectively. The proposed antenna was designed primarily for low-power CubeSat communication systems, which typically operate at modest transmit power levels (e.g., 0.5–2 W) due to tight power budgets in space platforms. With such high radiation efficiency, the vast majority of the input power is effectively converted into radiated energy, minimizing wasted energy as heat or surface wave losses. This directly reduces the power

that must be drawn from CubeSat's limited onboard energy supply to meet link budget requirements. In addition to the positive effect of having high efficiency, the high directive gain of the antenna provides a focused energy towards the target, reducing high-power transmission as well as signal dispersion. The low-profile, lightweight design also facilitates thermal management, as it avoids bulky structures that can trap heat or require active cooling. Regarding power handling and nonlinearity, the antenna was constructed from linear, passive materials that do not exhibit nonlinear behavior within the typical CubeSat operating power range. Given the passive MTS and the absence of active components in the antenna structure, nonlinearity or RF breakdown is not expected under standard operational conditions. However, should higher power applications be pursued, material breakdown thresholds and thermal effects could be investigated further.

The flower-like MTS, composed of coffee bean-shaped arrays and integrated with substrates of varying permittivity, enables precise control of electromagnetic waves, resulting in efficient leaky-wave propagation and beamsteering capabilities without the need for mechanical components. This design reduces complexity and weight while enhancing mission flexibility by allowing frequency- or phase-dependent beamsteering for the dynamic tracking of ground stations or inter-satellite links. Moreover, since the demand for higher data rates is growing in applications such as Earth observations and inter-satellite communications, the dual-port configuration of the proposed MIMO antenna is beneficial. The proposed antenna's CP feature enhances signal integrity, even in the presence of misalignment issues in CubeSat missions. Therefore, all these characteristics make the proposed antenna a high-performance candidate for CubeSat communications, especially for LEO.

Author Contributions: T.S. designed the antenna, carried out the measurements, and wrote the first draft of this paper. S.K. and S.S. evaluated the findings and edited the first draft of this paper. All authors have read and agreed to the published version of the manuscript.

Data Availability Statement: All the required data are within the main text.

Conflicts of Interest: The authors declare no conflicts of interest.

References

1. Siddique, I. Small Satellites: Revolutionizing Space Exploration and Earth Observation. *Eur. J. Adv. Eng. Technol.* **2024**, *11*, 118–12411.
2. Pozar, D.M. *Microwave Engineering*, 4th ed.; University of Massachusetts at Amherst: Amherst, MA, USA; John Wiley & Sons, Inc.: Hoboken, NJ, USA, 2012.
3. Balanis, C.A. *Antenna Theory: Analysis and Design*; John Wiley and Sons: Hoboken, NJ, USA, 2016.
4. Liu, S.; Theoharis, P.I.; Raad, R.; Tubbal, F.; Theoharis, A.; Iranmanesh, S.; Abulgasem, S.; Khan, M.U.A.; Matekovits, L. A Survey on CubeSat Missions and Their Antenna Designs. *Electronics* **2022**, *11*, 2021. [CrossRef]
5. Available online: https://www.itu.int/hub/2023/11/frequency-coordination-for-satellite-radio-services-in-s-x-and-ka-bands/?utm_source=chatgpt.com (accessed on 7 November 2023).
6. Chen, Y.; Qi, D.; Li, C. A Deep Learning Framework for Evaluating the Over-the-Air Performance of the Antenna in Mobile Terminals. *Sensors* **2024**, *24*, 5646. [CrossRef] [PubMed]
7. Aziz, R.S.; Koziel, S. A compact tri-band omnidirectional antenna design for CubeSat applications. *Sci. Rep.* **2025**, *15*, 11908.
8. Seo, S.; Kim, W.; Park, H.; Seo, Y.; Park, D.; Kim, H.; Lee, K.; Lee, H.; Kahng, S. Directivity Improved Antenna with a Planar Dielectric Lens for Reducing the Physical Size of the On-Vehicle Communication System. *Sensors* **2024**, *24*, 6831. [CrossRef]

9. González-Ovejero, D.; Mahmoud, A.; Morvan, X.; Ettorre, M.; Sauleau, R.; Maci, S. Metal-only modulated metasurface antenna for Cubesat platforms. In Proceedings of the 2019 IEEE International Symposium on Antennas and Propagation and USNC-URSI Radio Science Meeting, Atlanta, GA, USA, 7–12 July 2019.

10. Veljovic, M.J.; Skrivervik, A.K. Aperture-coupled low-profile wideband patch antennas for CubeSat. *IEEE Trans. Antennas Propag.* **2019**, *67*, 3439–3444.

11. Palacios, O.F.G.; Vargas, R.E.D.; Perez, J.A.H.; Erazo, S.B.C. S-Band Koch Snowflake Fractal Antenna For CubeSats. In Proceedings of the IEEE ANDESCON, Arequipa, Peru, 19–21 October 2016; pp. 1–4.

12. Lokman, A.H.; Soh, P.J.; Azemi, S.N.; Jamlos, M.F.; Al-Hadi, A.A.; Chalermwisutkul, S.; Kkaraekthalin, P. Compact Circularly Polarized S-Band Antenna for Pico-Satellites. In Proceedings of the 2017 International Symposium on Antennas and Propagation (ISAP), Phuket, Thailand, 30 October–2 November 2017; pp. 1–2.

13. Liu, S.; Raad, R.; Chin, K.-W.; Tubbal, F.E.M. Dipole Antenna Array Cluster for CubeSats. In Proceedings of the 10th International Conference on Signal Processing and Communication Systems (ICSPCS), Surfers Paradise, Australia, 19–21 December 2016; pp. 1–4.

14. Raza, A.; Adnan, M.; Maryam, H.; Mukhtar, M. Microstrip patch antenna fabricated and simulated results for S-Band, C-band and X-band antenna for space and communication applications. *Braz. J. Dev.* **2024**, *10*, e70809.

15. Samsuzzaman, M.; Islam, M.T. Inverted S-Shaped Compact Antenna for X-Band Applications. *Sci. World J.* **2014**, *2014*, 604375.

16. Arockia, P.; Mercy, M.; Wilson, K.S.J. High Gain Miniaturized Multi-band Microstrip Patch Antenna Using Slot-Cutting Techniques for C, and X Band Applications. *PriMera Sci. Eng.* **2023**, *2*, 53–65.

17. Mathur, P.; Kumar, G. Antenna at S-Band as Ground for Array at X-Band in Dual Frequency Antenna at S/X-Bands. *Prog. Electromagn. Res. Lett.* **2017**, *71*, 15–22.

18. Mishra, G.; Sharma, S.K.; Chieh, J.-C.S. A circular polarized feed horn with inbuilt polarizer for offset reflector antenna for W-band CubeSat applications. *IEEE Trans. Antennas Propag.* **2018**, *67*, 1904–1909.

19. Mathur, P.; Kumar, G. Dual-frequency microstrip antenna at S and X bands with higher-order mode suppression technique. *IET Microw. Antennas Propag.* **2018**, *12*, 583–587.

20. Buendía, V.G.; Podilchak, S.K.; Liberto, S.; Walkinshaw, T.; Constantinides, C.; Anagnostou, D.E.; Goussetis, G.; Van Der Vorst, M. Compact and Planar End-Fire Antenna for PicoSat and CubeSa Platforms to Support Deployable Systems. *IEEE Open J. Antennas Propag.* **2022**, *3*, 1341–1350.

21. Kuznetcov, M.V.; Podilchak, S.K.; Poveda-Garc, M.; Hilario, P.; Alistarh, C.A.; Goussetis, G.; G'omez-Tornero, J.L. Compact Leaky-Wave SIW Antenna with Broadside Radiation and Dual-Band Operation for CubeSats. *IEEE Antennas Wirel. Propag. Lett.* **2021**, *20*, 2125–2129.

22. Li, X.; Wang, J.; Goussetis, G.; Wang, L. Circularly Polarized High Gain Leaky-Wave Antenna for CubeSat Communication. *IEEE Trans. Antennas Propag.* **2022**, *70*, 7612–7624.

23. De, R.; Abegaonkar, M.P.; Basu, A. A broadband circularly polarized Fabry Perot antenna with spatially separated superstrate area excitation for CubeSat applications. *Sci. Rep.* **2023**, *13*, 11224.

24. Tubbal, F.; Raad, R.; Chin, K.-W.; Matekovits, L.; Butters, B.; Dassano, G. A high gain S-band slot antenna with MSS for CubeSat. *Ann. Telecommun.* **2019**, *74*, 223–237.

25. Kumar, M.V.; Sharma, D. A metasurface antenna with beam steering capabilities for radio frequency energy harvesting. *Comput. Electr. Eng.* **2024**, *118*, 109443.

26. Boyarsky, M.; Sleasman, T.; Imani, M.F.; Gollub, J.N.; Smith, D.R. Electronically steered metasurface antenna. *Sci. Rep.* **2021**, *11*, 4693.

27. Jahangiri, M.; Soleimani, H.; Soleimani, M. Beam steering by two vertically faced metasurfaces using polarization free unit cells with three operating modes. *Sci. Rep.* **2025**, *15*, 394.

28. Zhang, Y.; Tang, S.; Rao, J.; Chiu, C.-Y.; Chen, X.; Murch, R. A Dual-Port Dual-Beam Pattern-Reconfigurable Antenna With Independent 2-D Beam-Scanning. *IEEE Trans. Antennas Propag.* **2024**, *72*, 7628–7643.

29. Beiranvand, B.; Mirzavand, R. Enhancing wireless applications through reconfigurable electromechanical reflectarray antenna design for beam steering. *Sci. Rep.* **2024**, *14*, 30140.

30. Du, H. Broadband Fixed-Beam Leaky-Wave Antenna with Consistent and High Gain Based on Ridge Gap Waveguide. *IEEE Antennas Wirel. Propag. Lett.* **2022**, *21*, 1925–1929.

31. Trzebiatowski, K.; Kalista, W.; Rzymowski, M.; Kulas, Ł.; Nyka, K. Multibeam Antenna for Ka-Band CubeSat Connectivity Using 3-D Printed Lens and Antenna Array. *IEEE Antennas Wirel. Propag. Lett.* **2022**, *21*, 2244–2248.

32. Ali, S.M.; Jeoti, V.; Saeidi, T.; Wong, P.W. Design of compact microstrip patch antenna for WBAN applications at ISM 2.4 GHz. *Indones. J. Electr. Eng. Comput. Sci.* **2019**, *15*, 1509–1516.

33. Ali bakhshikenari, M.; Virdee, B.S.; See, C.H.; Abd-Alhameed, R.A.; Falcone, F.; Limiti, E. High-isolation leaky-wave array antenna based on CRLH-metamaterial implemented on SIW with ±30 frequency beam-scanning capability at millimetre-waves. *Electronics* **2019**, *8*, 642. [CrossRef]

34. Saeidi, T.; Al-Gburi, A.J.A.; Karamzadeh, S. A miniaturized full-ground dual-band MIMO spiral button wearable antenna for 5G and sub-6 GHz communications. *Sensors* **2023**, *23*, 1997. [CrossRef]

35. Faenzi, M.; Minatti, G.; González-Ovejero, D.; Caminita, F.; Martini, E.; Della Giovampaola, C. Metasurface Antennas: New Models, Applications and Realizations. *Sci. Rep.* **2019**, *9*, 10178.

36. Landy, N.I.; Sajuyigbe, S.; Mock, J.J.; Smith, D.R.; Padilla, W.J. Perfect Metamaterial Absorber. *Phys. Rev. Lett.* **2008**, *100*, 207402.

37. Baqir, M.A.; Latif, H.; Altintas, O.; Akhtar, M.N.; Karaaslan, M.; Server, H.; Hameed, M.; Idrees, N.M. Fractal metamaterial based multi-band absorber operating in 5G regime. *Optik* **2022**, *266*, 169626.

38. Dutta, R.K.; Bandyopadhyay, B.; Jaiswal, R.K.; Srivastava, K.V. Beamforming of a Linear Antenna Array Using Reconfigurable Frequency Selective Surface. In Proceedings of the 2023 IEEE Microwaves, Antennas, and Propagation Conference (MAPCON), Ahmedabad, India, 11–14 December 2023.

39. Ta, S.X.; Le, V.D.; Nguyen, K.K.; Dao-Ngoc, C. Planar circularly polarized X-band array antenna with low sidelobe and high aperture efficiency for small satellites. *Int. J. RF Microw. Comput. Aided Eng.* **2019**, *29*, e21914.

40. Hodges, R.E.; Chahat, N.; Hoppe, D.J.; Vacchione, J.D. A Deployable High-Gain Antenna Bound for Mars. *IEEE Antennas Propag. Mag.* **2017**, *59*, 39–49.

41. Zarbakhsh, S.; Akbari, M.; Farahani, M.; Ghayekhloo, A.; Denidni, T.A.; Sebak, A.-R. Optically transparent subarray antenna based on solar panel for CubeSat application. *IEEE Trans. Antennas Propag.* **2020**, *68*, 319–328.

42. Rabie, M.M.; El-Henawy, H.; El-Hefnawy, F.; Ibrahim, F. Transparent Microstrip GPS Antenna for Cubesat Applications. In Proceedings of the 17th International Conference on Aerospace Sciences & Aviation Technology (ASAT-17), Cairo, Egypt, 11–13 April 2017.

43. Saeidi, T.; Saleh, S.; Mahmood, S.N.; Timmons, N. Ahmed Jamal Abdullah Al-Gburi, Faroq Razzaz, Saeid Karamzadeh, 'High Gain Multi-band Circularly Polarized Wearable Leaky Wave Zipper MIMO Antenna. *Heliyon* **2024**, *10*, e33024.

44. Da Silva, W.G.; Campos, A.L.P.S.; Guerra, J.R.F. A Compact Dual-Band UHF Microstrip Patch Antenna for CubeSat Applications. *J. Commun. Inf. Syst.* **2021**, *36*, 166–172.

45. Abulgasem, S.; Tubbal, F.; Raad, R.; Theoharis, P.I.; Lu, S.; Iranmanesh, S. Antenna Designs for CubeSats: A Review. *IEEE Access* **2021**, *9*, 45289–45324.